A-site cation size effect on oxygen octahedral rotations in acentric Ruddlesden-Popper alkali rare-earth titanates

Hirofumi Akamatsu,[1,*] Koji Fujita,[2,†] Toshihiro Kuge,[2] Arnab Sen Gupta,[3] James M. Rondinelli,[4] Isao Tanaka,[5] Katsuhisa Tanaka,[2] and Venkatraman Gopalan[3,‡]

[1]*Department of Applied Chemistry, Kyushu University, Motooka, Fukuoka 819-0395, Japan*
[2]*Department of Material Chemistry, Kyoto University, Nishikyo, Kyoto 615-8510, Japan*
[3]*Materials Research Institute and Department of Materials Science and Engineering, Pennsylvania State University, MSC Building, University Park, Pennsylvania 16802, USA*
[4]*Department of Materials Science and Engineering, Northwestern University, Evanston, Illinois 60208, USA*
[5]*Department of Materials Science and Engineering, Kyoto University, Sakyo, Kyoto 606-8501, Japan*

We demonstrate inversion symmetry breaking induced by oxygen octahedral rotations in layered perovskite oxides $KA_R TiO_4$ (A_R = rare earth) using a combined experimental and theoretical approach including synchrotron x-ray diffraction, optical second harmonic generation, and first-principles lattice dynamics calculations. We experimentally find an interesting but counterintuitive phenomenon, i.e., the acentric-to-centric phase transition temperatures for K family are higher than those for previously reported Na family, in contrast to expectations based on the Goldschmidt tolerance factor, where the octahedral rotation instability toward the acentric phases would reduce with an increase in the radius of A-site alkali metal ions. Our detailed analysis of first-principles calculations for $A_A A_R TiO_4$ (A_A = Na, K, Rb) reveals that the alkali metal and rare-earth ions play quite different roles in driving the octahedral rotations. Since rare-earth ions attract oxide ions more strongly than alkali metal ions due to the higher valence of the former in comparison with the latter (A_R^{3+} vs A_A^+), the optimization of coordination environment of rare-earth ions is the primary driving force of the octahedral rotations. Alkali metal ions serve to impose "bond strains" parallel to the layers, playing a secondary role in the octahedral rotations. Incorporation of large alkali metal ions generates a significant in-plane biaxial bond strain in $A_R O$ and TiO_2 layers through the expanded $A_A O$ layers, and thereby facilitates the octahedral rotations because of the otherwise highly underbonding of rare-earth ions. Thus, the effect of A-site alkali metal size on the octahedral rotation instability can be explained in terms of the interlayer lattice mismatch. This understanding allows us to propose a geometric descriptor governing the structural instability in $A_A A_R TiO_4$ layered perovskites. We believe that control over the interlayer lattice mismatch could be a useful strategy to tune the octahedral rotations in layered compounds.

I. INTRODUCTION

Rotations of rigid structural units such as anion polyhedra coordinating cations are one of the most ubiquitous structural distortions in inorganic compounds. In particular, rotation and tilt of oxygen-coordinated octahedra in perovskite-related oxides have been extensively studied for many decades from viewpoints of fundamental science such as crystallochemistry, group theory, and density functional theory (DFT) [1–6], and have received considerable attention due to emerging phenomena such as metal-insulator phase transitions [7–9]. The driving force for octahedral rotations in perovskites is, to a first approximation, a need to optimize the anion coordination environment of underbonded A-site cations. The ionic size dependence of the instability for octahedral rotations and tilts is often discussed in terms of Goldschmidt tolerance

factor [10], which is defined based on a geometric condition in accommodating the A- and B-site cations coordinated by anions into aristotype perovskite structures as follows:

$$\tau = \frac{(r_A + r_X)}{\sqrt{2}(r_B + r_X)}, \qquad (1)$$

where r_A, r_B, and r_X are ionic radii of A- and B-site cations and anions, respectively. In the case of $\tau = 1$, the anion coordination environments for A- and B-site cations are ideal in the aristotype perovskite structures. When τ is smaller than unity and the BX_6 octahedra are rigid, rotations occur so as to optimize the A-X bond length and the coordination number. Indeed, the tolerance factor is a simple and good descriptor for the instability of rotations and tilts in simple perovskite oxides ABO_3. In particular, the tolerance factor explains well the A-site cation size dependence of octahedral rotation instability for a given B-site cation, while adopted rotation and tilt patterns and their magnitude are also dependent of the combinations of the valences of A- and B-site cations and the nature of the B-O bonding, i.e., ionicity and covalency [3].

*h.akamatsu@cstf.kyushu-u.ac.jp
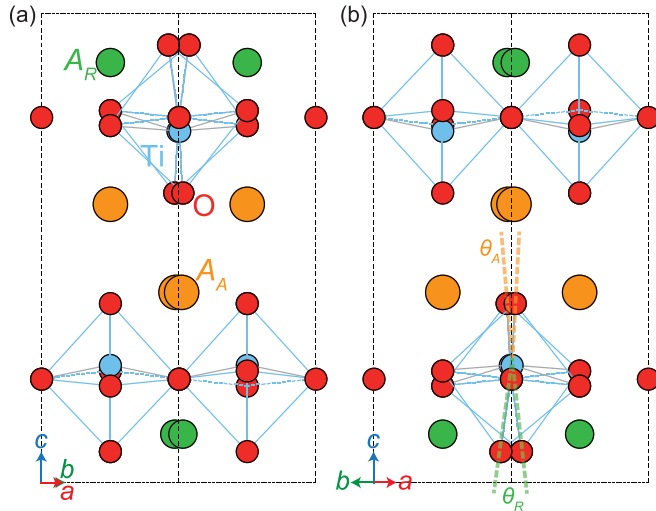†fujita.koji.5w@kyoto-u.ac.jp
‡vxg8@psu.edu

FIG. 1. Schematic illustration of crystal structure of $A_A A_R \text{TiO}_4$ with $P\bar{4}2_1m$ space-group symmetry viewed along (a) $[\bar{1}10]$ and (b) $[110]$ directions. Octahedral rotation angles θ_A and θ_R are defined.

There is renewed interest in acentricity driven by octahedral rotations and tilts. Inversion symmetry can be lifted by octahedral rotations and tilts in layered perovskite oxides, although this is not the case with simple $AB\text{O}_3$ perovskites [11–22]. An electric polarization induced via a trilinear coupling to two nonpolar modes, termed "hybrid improper ferroelectricity," has been experimentally demonstrated in a couple of layered perovskite oxides [11,23–30]. Recently, the acentricity of A-site ordered Ruddlesden-Popper (RP) phases, $A_A A_R \text{TiO}_4$ (A_A = H, Li, and Na, A_R = rare earth) has been also reported [31–33]. One can see a bilayer ordering of two kinds of A-site cations and the octahedral rotations represented by $(\Phi 00)(0\Phi 0)$ in Aleksandrov notation [34] in a so-called K_2NiF_4-type structure (Fig. 1). The inversion symmetry is lifted by the octahedral rotation, converting parent $P4/nmm$ to noncentrosymmetric nonpolar $P\bar{4}2_1m$ structures (Fig. 1) [20,21]. For these series, synchrotron x-ray diffraction (XRD) and optical second harmonic generation (SHG) revealed higher acentric-to-centric transition temperatures for the compounds with smaller A_R ions, and first-principles DFT calculations clarified that the structural stabilization by octahedral rotations increases with a decrease in the ionic radius of A_R ions; the smaller A_R ions facilitate the octahedral rotations [31–33]. These results are consistent with the tolerance factor argument as described in Eq. (1), which is applicable to K_2NiF_4-type structures as originally formulated [35].

In this work, we extend the series to different alkali ions, focusing on $A_A A_R \text{TiO}_4$ with A_A = K and Rb. Although the synthesis and structural properties of $\text{K}A_R\text{TiO}_4$, with A_R = La, Nd, Sm, Eu, Gd, and Dy, have been reported so far [36–38], previous diffraction studies have assigned the crystal symmetry of $\text{K}A_R\text{TiO}_4$ to a centric $Pbcm$ space group, which encompasses $(\Phi\Phi 0)$-type of octahedral rotations. Through DFT calculations, however, we here predict their ground-state structures to comprise $(\Phi 00)(0\Phi 0)$-type octahedral rotations, leading to an acentric $P\bar{4}2_1m$ space group, as in $\text{Na}A_R\text{TiO}_4$ [31] and $\text{Li}A_R\text{TiO}_4$ [32]. XRD and optical SHG measurements experimentally confirm the prediction of crystal symmetry for

$\text{K}A_R\text{TiO}_4$ with A_R = Sm and Eu (Sec. III A). We also theoretically show that the octahedral rotation instability grows when the A_A ions become larger, which is opposite to a simple tolerance factor argument [Eq. (1)]. To experimentally verify this prediction, we compare the acentric-to-centric phase transition temperatures between K and Na families through variable-temperature XRD and SHG (Sec. III B). Detailed crystallochemical analysis of the DFT calculation results allows us to elucidate a mechanism behind the inconsistency with the tolerance factor argument, highlighting that the A_A (Sec. III C) and A_R ions (Sec. III D) play different roles in the octahedral rotations: A_R ions, which have a higher charge than A_A ions, work to induce exclusively the octahedral rotations due to the stronger electrostatic interaction between A_R and oxide ions. Namely, a need to optimize the coordination environment of underbonded A_R ions is the primary driving force for octahedral rotations. On the other hand, the A_A ions serve to impose biaxial tensile strains in the in-plane direction of $A_R\text{O}$ and TiO_2 layers due to interlayer lattice mismatch, and so the large A_A ions promote the octahedral rotations; otherwise A_R ions would be highly underbonded. Thus, the alkali metal size effect on octahedral rotations is opposite to the trend expected from the tolerance factor argument. In the last part of this paper (Sec. III E), a geometric descriptor regarding the rotation instability in the present layered perovskites is proposed.

II. METHODS

A. Computational details

First-principles DFT calculations were performed using the projector augmented-wave (PAW) method [39,40] and the PBEsol functional [41–43] as implemented in the VASP code [44–47]. The standard PAW cutoffs were used with a plane-wave cutoff energy of 550 eV. The following states were described as valence electrons: $2p^6$, $3s^1$ for Na; $3p^6$, $4s^1$ for K; $4p^6$, $5s^1$ for Rb; $4s^2$, $4p^6$, $4d^1$, $5s^2$ for Y; $5s^2$, $5p^6$, $5d^1$, $6s^2$ for La, Nd, and Sm; $5p^6$, $5d^1$, $6s^2$ for Gd, Dy, and Ho; $3s^2$, $3p^6$, $3d^2$, $4s^2$ for Ti; and $2s^2$, $2p^4$ for O. Here, $4f$ states were not treated as valence electrons, but we confirmed that qualitatively similar results were obtained when the $4f$ states were explicitly included as valence states. Γ-centered k-point mesh sampling of $4 \times 4 \times 2$ was used for $\sqrt{2} \times \sqrt{2} \times 1$ supercells of the primitive cells of $P4/nmm$ structures with 28 atoms, which are necessary to represent the $P\bar{4}2_1m$ structure since this structure is derived by freezing the octahedral rotation mode at the Brillouin-zone boundary $M(\frac{1}{2}\frac{1}{2}0)$ point of the $P4/nmm$ structures. The lattice constants and internal coordinates were optimized until the residual stress and forces converged to 0.01 GPa and 1 meV/Å, respectively.

The lattice dynamical properties were calculated using the PHONOPY code from the calculated DFT force constants [48]. Stable structures were searched for by finding unstable phonon modes, according to a method described by Togo and Tanaka [49]: First, phonon frequencies are calculated at the Brillouin-zone center and boundaries for the aristotype $P4/nmm$ structures. If no unstable phonon modes are found, the structure is found to be dynamically stable, and then the structural search is finished. If unstable phonon modes

are found, the parent structure is distorted according to the eigenvectors of the unstable phonon modes so as to obtain "children" structures with lower total energy and symmetry, followed by structural optimization. Then, phonon calculations are performed for the well-optimized "children" structures. In case that unstable phonon modes are found for them, this procedure is repeated. Otherwise, the structure is found to be dynamically stable. The treelike diagram representing the structural evolution is completed when it is found that there is no unstable phonon mode at all.

B. Experimental procedures

Polycrystalline powder samples of KA_RTiO$_4$ for A_R = Sm and Eu were prepared via a solid-state reaction method. Our synthesis conditions are similar to those reported in Ref. [37]. Reagent-grade K$_2$CO$_3$, Sm$_2$O$_3$, Eu$_2$O$_3$, and TiO$_2$ powders were used as starting materials. The Sm$_2$O$_3$ and Eu$_2$O$_3$ powders were heated prior to weighting at 900 °C for 12 h to eliminate water and carbon dioxide adsorbed on the powders. A 50-mol% excess amount of K$_2$CO$_3$ was added to a mixture of the starting materials to compensate for the loss due to the K evaporation during heating. The mixtures were ground for 30 min with an agate mortar, followed by another 30 min grinding with acetone. About 0.5 g pellets of the mixtures were put on an alumina plate, covered with an alumina lid, and then calcinated at 850 °C for 30 min in an electric furnace. The resultant pellets were ground, thoroughly mixed, pelletized again, and then sintered at 850 °C for 6 h.

The phase purity of the resultant powders was checked by laboratory XRD. To reinvestigate the structures of the compounds, high-resolution synchrotron XRD patterns were taken with a Debye-Scherrer camera at the BL02B2 beamline of SPring-8. We used an x-ray beam monochromated at λ = 0.774 964 Å. Rietveld refinements were performed using the RIETAN-FP code [50]. In order to confirm the acentricity, optical SHG measurements were performed in reflection geometry with an 800-nm fundamental beam of Ti:sapphire laser (80-fs pulses and 1-kHz repetition rate) [31–33].

III. RESULTS AND DISCUSSION

A. Crystal structure determination

First, we searched for the ground-state structures for KYTiO$_4$ and RbYTiO$_4$ from the parent $P4/nmm$ structures using first-principles lattice dynamics calculations. Treelike diagrams constructed by the structural search are shown in the Supplemental Material [51]. We found that their ground-state structures are acentric $P\bar{4}2_1m$ structures (Fig. 1), which are obtained by the condensation of the M_1 modes corresponding to (Φ00)(0Φ0)-type octahedral rotations, as in NaYTiO$_4$ and LiYTiO$_4$ [31,32]. The $P\bar{4}2_1m$ structures show no further structural instability into any other polar phase, ruling out the possibility of ferroelectricity. The total energy of the $P\bar{4}2_1m$ structures for KYTiO$_4$ and RbYTiO$_4$ is lower by 50 and 58 meV per formula unit (f.u.), respectively, than that of the $Pbcm$ structures as reported previously for KA_RTiO$_4$ [36–38]. Figure 2 presents the total energies of the $P\bar{4}2_1m$ and $Pbcm$ structures relative to the parent $P4/nmm$ phase as a function of rare-earth ionic radius for (a) KA_RTiO$_4$ and (b) RbA_RTiO$_4$,
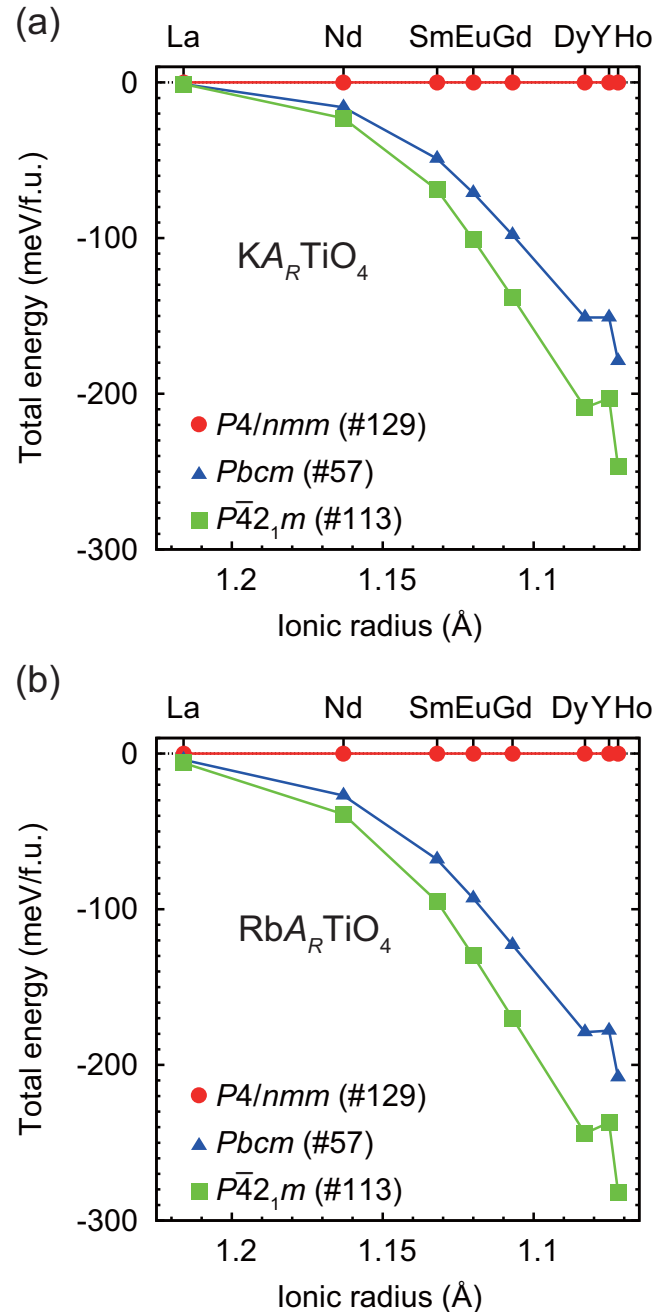

FIG. 2. Total energies of the $P\bar{4}2_1m$ and $Pbcm$ structures relative to the parent $P4/nmm$ phase as a function of ionic radius of rare earth for (a) KA_RTiO$_4$ and (b) RbA_RTiO$_4$.

revealing that the $P\bar{4}2_1m$ structures are the most stable for KA_RTiO$_4$ and RbA_RTiO$_4$ with A_R = La, Nd, Sm, Eu, Gd, Dy, and Ho as well as Y, as in NaA_RTiO$_4$ with A_R = rare earths smaller than La [31].

Next, we reinvestigated the structures of KA_RTiO$_4$ with A_R = Sm and Eu by synchrotron XRD. Figure 3 shows the XRD patterns along with fitting curves obtained by Rietveld refinements. The Rietveld refinements were performed against the XRD patterns taken at room temperature using both the $P\bar{4}2_1m$ and $Pbcm$ structural models. The XRD pattern for A_R = Sm fits well using the both models with a small
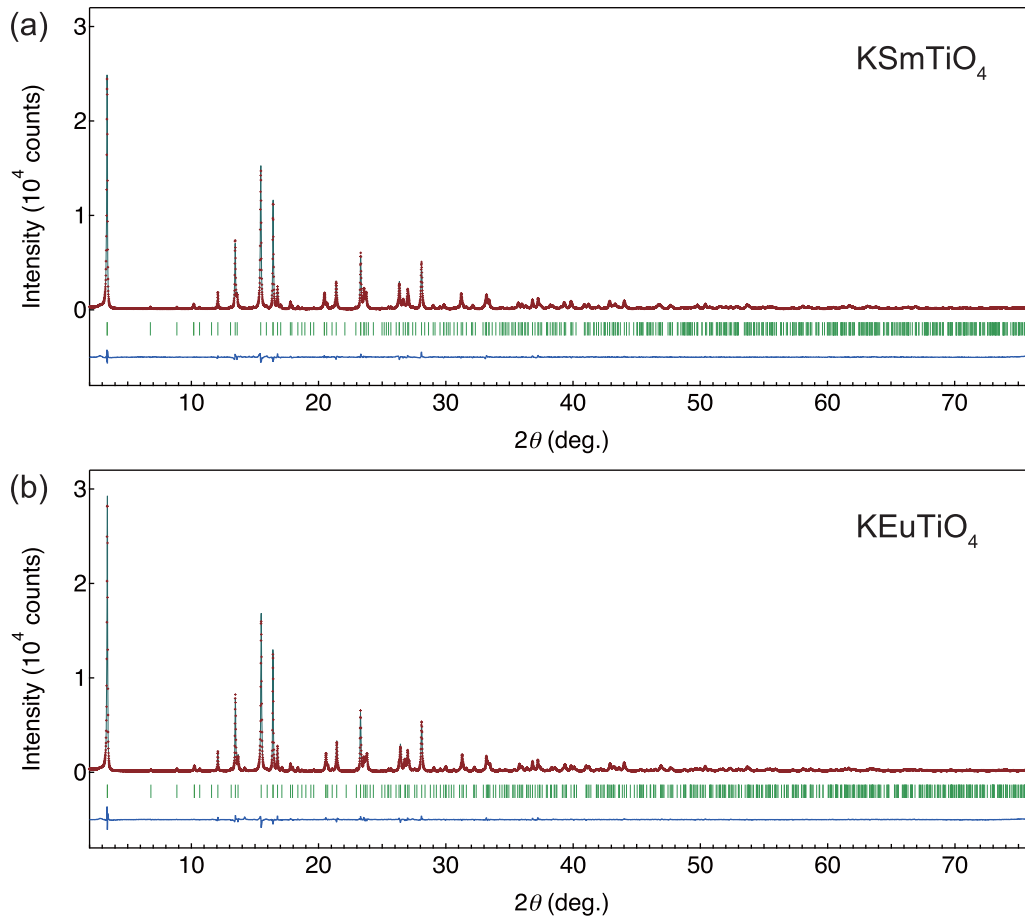
FIG. 3. Synchrotron XRD patterns of (a) KSmTiO$_4$ and (b) KEuTiO$_4$ collected at room temperature with x-ray of $\lambda = 0.774\,964$ Å and fitting curves obtained by Rietveld refinements using the $P\bar{4}2_1m$ models. The refined structural parameters are summarized in Table I.

reliability factor: $R_{\mathrm{wp}} = 7.531\%$ and 7.729% for the $P\bar{4}2_1m$ and *Pbcm* models, respectively. For $A_R =$ Eu, $R_{\mathrm{wp}} = 7.534\%$ and 7.748% for the $P\bar{4}2_1m$ and *Pbcm* models, respectively. Because of the similar reliability factors, we could not unambiguously determine the structures only in terms of the reliability factors in the Rietveld analysis of the XRD data. This is likely because the two structures are different just in the octahedral rotation patterns and there is a difficulty in refining the oxygen positions. As will be detailed in Sec. III B, both the compounds exhibit a significant SHG signal at room temperature, which provides evidence for their acentricity. Thereby, we identify their room-temperature structures as the acentric $P\bar{4}2_1m$ structures. The refined crystal-structure parameters for the $P\bar{4}2_1m$ models are summarized in Table I.

B. Octahedral rotation instability

Figure 4(a) maps the Goldschmidt tolerance factor onto the ionic radius of A_A and A_R ions tabulated by Shannon [52]. In the calculation of the tolerance factor, averaged ionic radii of the A_A and A_R ions are used as r_A in Eq. (1). The tolerance factor decreases linearly with a decrease in the ionic radius of the A-site cations according to Eq. (1). Figure 4(b) shows the total energies of the $P\bar{4}2_1m$ structures with respect to those of the parent structures, which correspond to the energy gain by the octahedral rotations. The lower total energy indicates

stronger octahedral rotation instability. For a given A_A ion, the instability becomes stronger when A_R ions get smaller, as expected from the tolerance factor argument. For a given A_R ion, on the other hand, A_A ions have an opposite effect on the instability. We see that the large A_A ions enhance the octahedral rotation instability; the energy gain by the octahedral rotation is smaller for the Na family than for the K and Rb families, although the influence of ionic radius of alkali metals is much smaller than that of rare earths. Thus, the alkali metal size effect is inconsistent with the tolerance factor argument.

Figures 5(a) and 5(b) present the temperature dependence of SHG signal for A_ASmTiO$_4$ ($A_A =$ Na and K) and A_AEuTiO$_4$, respectively. All of the compounds exhibit a significant SHG signal at room temperature, indicating their acentricity. Thereby, we definitely conclude that their room-temperature phases adopt the acentric $P\bar{4}2_1m$ structures. The temperature-dependent SHG intensity for the K compounds does not reach zero in slope and still decreases when the SHG signal for the Na compounds falls to zero upon heating. The higher phase transition temperatures for the larger A_A ions are in a good agreement with the DFT calculation results showing that the energy gain by the octahedral rotations increases with an increase in the size of alkali metal [see Fig. 4(b)]. The inset of Fig. 5(a) plots the temperature variation of XRD peak area of $\frac{1}{2}\frac{1}{2}1$ superlattice reflection with respect to the parent

TABLE I. Crystallographic data of KA_RTiO_4 (A_R = Sm, Eu) derived from Rietveld analyses against synchrotron XRD patterns at room temperature. The wavelength of x ray is 0.774 964 Å. Isotropic atomic displacement parameters B were fixed to 0.1 for Ti and O during the refinements to avoid convergence to unphysical values.

Sample	Atom	Site	x	y	z	B (Å^2)
KSmTiO$_4$	K	4e	0.7615(5)	$x - \frac{1}{2}$	0.4047(2)	0.60(4)
$P\bar{4}2_1m$ (No. 113)	Sm	4e	0.7638(1)	$x - \frac{1}{2}$	0.1031(1)	0.14(2)
a = 5.42420(7) Å	Ti	4e	0.7538(3)	$x - \frac{1}{2}$	0.7494(2)	0.1
c = 13.08660(28) Å	O1	2c	0	$\frac{1}{2}$	0.7970(16)	0.1
R_{wp} = 7.53%	O2	4d	0	0	0.7776(15)	
R_p = 5.22%	O3	2c	0	$\frac{1}{2}$	0.2325(21)	
S_{fit} = 1.44	O4	4e	0.7049(9)	$x - \frac{1}{2}$	0.9331(6)	
	O5	4e	0.7715(10)	$x - \frac{1}{2}$	0.6146(5)	
KEuTiO$_4$	K	4e	0.7633(5)	$x - \frac{1}{2}$	0.4045(2)	0.65(5)
$P\bar{4}2_1m$ (No. 113)	Eu	4e	0.7661(1)	$x - \frac{1}{2}$	0.1028(1)	0.17(2)
a = 5.42776(7) Å	Ti	4e	0.7545(4)	$x - \frac{1}{2}$	0.7505(2)	0.1
c = 13.01638(25) Å	O1	2c	0	$\frac{1}{2}$	0.7951(17)	0.1
R_{wp} = 7.53%	O2	4d	0	0	0.7795(16)	
R_p = 4.99%	O3	2c	0	$\frac{1}{2}$	0.2291(21)	
S_{fit} = 1.48	O4	4e	0.7032(9)	$x - \frac{1}{2}$	0.9345(6)	
	O5	4e	0.7716(10)	$x - \frac{1}{2}$	0.6170(5)	

$P4/nmm$ structure for NaSmTiO$_4$ and KSmTiO$_4$. It should be noted that the intensity of superlattice reflection is relevant to an order parameter for the $P4/nmm$ to $P\bar{4}2_1m$ phase transition [31–33]. One can see clearly the higher phase transition temperature for KSmTiO$_4$ than for NaSmTiO$_4$. Thus, the stronger octahedral rotation instability for the compounds with larger A_A ions is experimentally verified.

C. Dominant factor for the octahedral rotations

Hereafter, we focus on the A_A-ion size effects unexpected from the tolerance factor argument. Specifically, we attempt to untangle the puzzling question as to why the octahedral rotation instability is increased for A_A ions of a larger size, while it is decreased for A_R ions of a larger size. In order to figure out the main driving force for the octahedral rotation in the $A_AA_RTiO_4$ system, let us see the changes in structural features resulting from the octahedral rotation, which are extracted from the DFT calculation results for the initial ($P4/nmm$) and final ($P\bar{4}2_1m$) structures. In general, octahedral rotations involve the optimization of coordination environment of underbonded A-site cations via the reduction of A-X bond length and coordination number [3–5]. The changes in bond length between cations and O ions could hint to the driving force of octahedral rotations. In particular, it is instructive to focus on the bonds that are significantly shortened by the octahedral rotations.

In Fig. 6(a), all the bonds between the cations and O ions are defined in a schematic of the $P\bar{4}2_1m$ structure. Nine bonds between the A-site cations and O ions in the parent $P4/nmm$ structure are classified into three types: A-O ax (×1), eq (×4), and dg (×4) bonds, which correspond to the bonds to the O ions in the axial, equatorial, and diagonal directions, respectively. The four A-O eq bonds are split into eq(I) (×2) and eq(II) (×2) bonds due to symmetry lowering

by the rotation distortion, and the four A-O dg bonds into dg(I) (×1), dg(II) (×2), and dg(III) (×1) bonds. The Ti ions have five types of bonds in the $P\bar{4}2_1m$ structure: Ti-O ax(I), ax(II), eq(I), eq(II), and eq(III) bonds. As a example, Fig. 6(b) shows the changes in the length of all the bonds for NaYTiO$_4$. First, all the Ti-O bonds do not change so much, indicating that the TiO$_6$ octahedra are rather rigid. On the other hand, there are significant changes for the Na-O and Y-O bonds. In particular, the Na-O dg(I) and Y-O eq(I) bonds become shortened most significantly by the octahedral rotations. The Na and O ions forming the Na-O dg(I) bond come toward each other in the rotation distortion, and so do the Y and O ions forming the Y-O eq(I) bond.

We should take a close look at the changes in the two kinds of bonds for this series of compounds. The changes in the A_R-O eq(I) and A_A-O dg(I) bond lengths are presented as a function of the ionic radius of A_R for $A_AA_RTiO_4$ with A_A = Na, K, and Rb in Figs. 7(a) and 7(b), respectively. The magnitude of the A_R-O eq(I) bond length change becomes larger with decreasing size of A_R ions and increasing size of A_A ions. This trend is the same as that of the energy gain by octahedral rotations as shown in Fig. 4(b). The magnitude of the A_A-O dg(I) bond length change also gets larger with decreasing the size of A_R ions. When the A_R ions are small (A_R = Eu or smaller), however, the magnitude of the bond length change for A_A = Na is larger than those for A_A = K and Rb. This result indicates that the A_A-O dg(I) bond length change does not correlate well with the energy gain accompanied by the octahedral rotations, in contrast to the A_R-O eq(I) bond length change. Given the valence state of A_A and A_R ions (A_A^{1+} and A_R^{3+}), the A_R-O eq(I) bond length change can contribute much more to the energy gain by the octahedral rotations. From another chemical viewpoint, we consider that A_R ions, which are a harder acid compared to A_A ions, form stronger covalent bonds to oxide ions, which are a
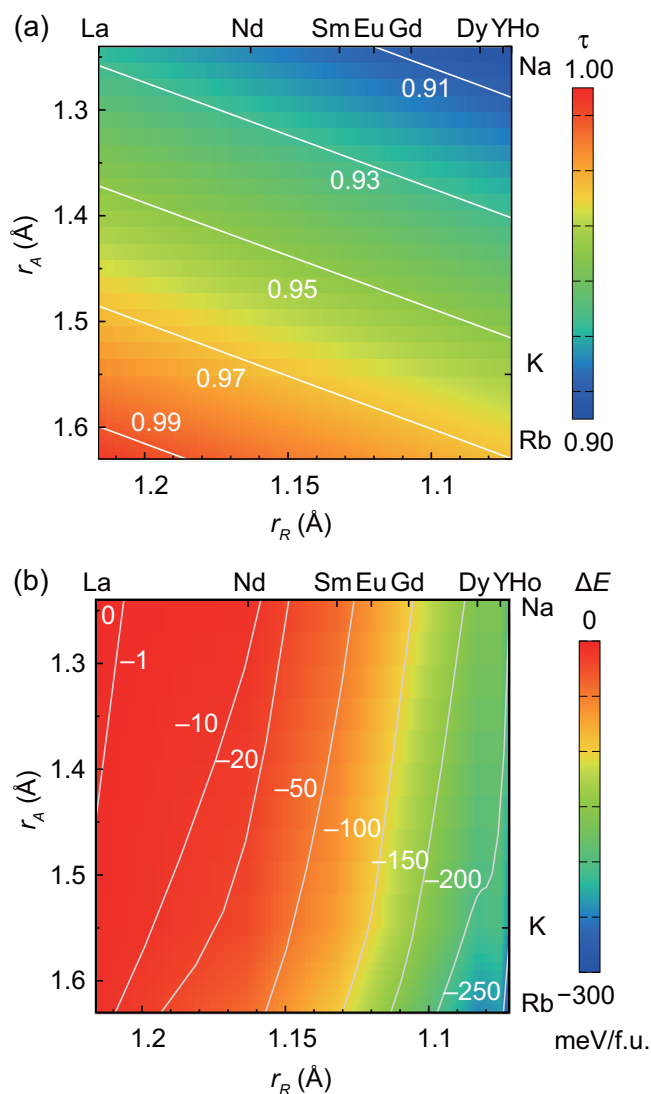
FIG. 4. (a) Goldschmidt tolerance factor τ and (b) total energy of $P\bar{4}2_1m$ structures relative to that of $P4/nmm$ parent structures as a function of ionic radius of alkali metal (vertical axis) and rare earth (horizontal).

FIG. 5. Temperature dependence of second harmonic generation for (a) $A_A\mathrm{SmTiO_4}$ and (b) $A_A\mathrm{EuTiO_4}$ with $A_A = \mathrm{Na}$ (yellow circles) and K (purple circles). The inset of (a) presents the temperature dependence of peak area of $(\frac{1}{2}\frac{1}{2}1)$ superlattice reflection with respect to the $P4/nmm$ parent structure. The arrows in (a) indicate the range in which the phase transitions are revealed to occur by the temperature-dependent superlattice reflection (see Ref. [31] for the temperature variation of synchrotron XRD patterns for NaSmTiO$_4$).

hard base. Also note that there are two equivalent A_R-O eq(I) bonds, doubling the energy contribution. Here, we examine in more detail the correlation between the energy gain and the rotation-induced bond length change in cation-oxygen pairs as shown in Fig. 6. The total energies of the $P\bar{4}2_1m$ phases relative to the parent $P4/nmm$ phases are plotted in Fig. 8 as a function of the bond length change induced by the the rotation distortions; note that Fig. 8 presents the results of all the compositions, i.e., $A_A A_R\mathrm{TiO_4}$ with $A_A = \mathrm{Na}$, K, and Rb, and $A_R = \mathrm{La}$, Nd, Sm, Eu, Gd, Dy, Y and Ho. It is found that several cation-oxygen bonds [e.g., A_A-O dg(I) and A_R-O eq(I)] lead to a decrease in the total energy through the shortening of the bond length. Among them, the A_R-O eq(I) bond length change has the closest correlation with the energy gain concomitant with the rotation distortion. It seems that how strongly the A_R ions attract oxide ions is responsible for the octahedral rotation instability.
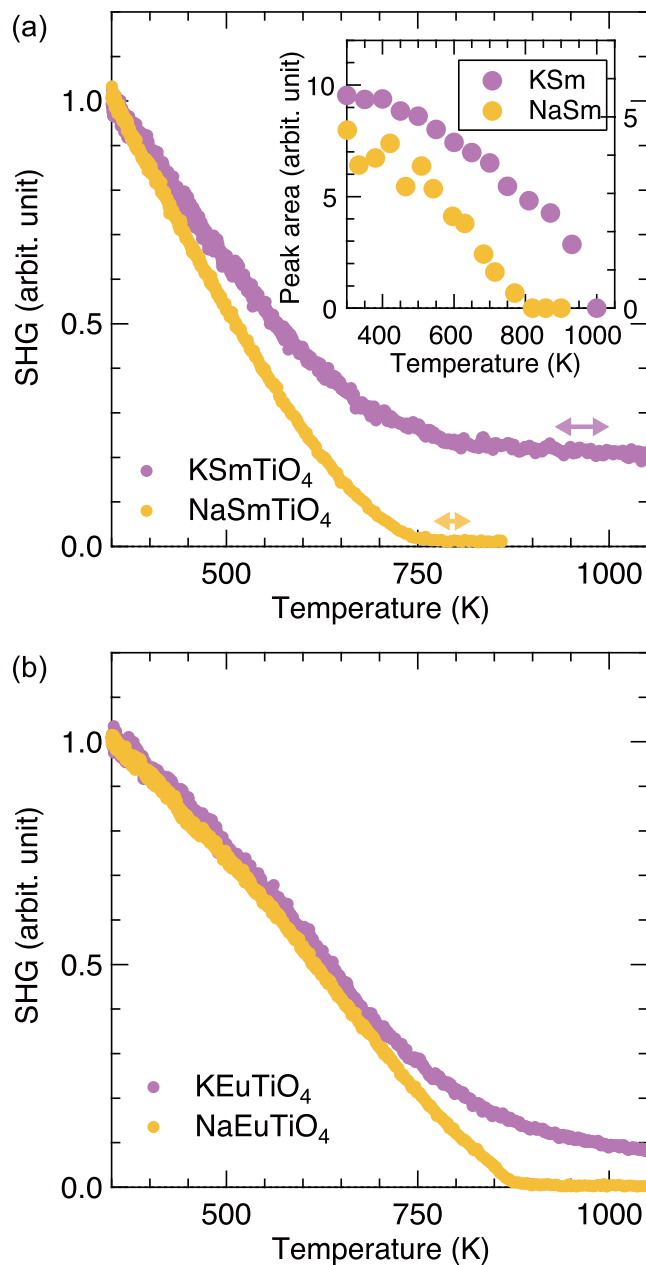
This idea is corroborated by the A-site cation size dependence of the octahedral rotation angles. Figures 7(c) and 7(d) show the A-site cation dependence of the octahedral rotation angles θ_R and θ_A, respectively, which are defined in Fig. 1(b). The θ_R angle becomes larger as A_R ions become smaller and A_A ions become larger; the octahedral rotation instability correlates strongly with the θ_R angle. On the other hand, the θ_A
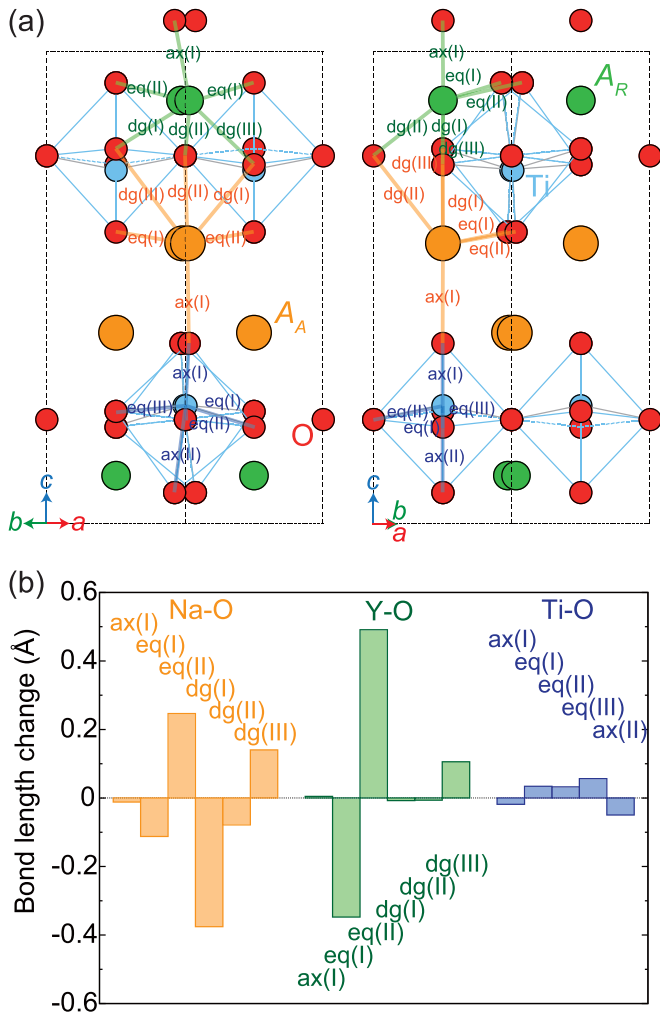
FIG. 6. (a) Schematic of the $P\bar{4}2_1m$ structure for A_AA_RTiO$_4$ viewed along [110] and [$\bar{1}$10] directions, in which bonds between cations and oxide ions are defined. The bonds to the oxide ions in the axial, equatorial, and diagonal directions are denoted as "ax," "eq," and "dg," respectively. (b) The bond length change caused by the $(\Phi00)(0\Phi0)$-type of octahedral rotations for NaYTiO$_4$.

FIG. 7. The change in the length of (a) A_R-O eq(I) and (b) A_A-O dg(I) bonds and the octahedral rotation angle, (c) θ_R and (d) θ_A, defined in the inset of Fig. 1(b), as a function of A_R ionic radius for A_AA_RTiO$_4$ with A_A = Na (yellow circles), K (purple squares), and Rb (bluish-green triangles).

angle increases with decreasing the size of A_R ions, but its A_A-ion dependence is not straightforward and does not correlate strongly with the octahedral rotation instability, as well as the A_A-O dg(I) bond length change. Thus, the optimization of the coordination environment of the A_R ions is the primary driving force of the octahedral rotations, and the A_A ions play a secondary role in the octahedral rotations.

D. Origin of the effect of alkali metal size

Now, we discuss how large A_A ions enhance the octahedral rotation instability contrary to the simple tolerance factor argument. As discussed in Sec. III C, the role of A_A ions in the structural instability is not clear in terms of the change in the bond length. Here, we consider "electrostatic chemical strain" or "bond strain" [53,54] caused by the replacement of Na ions in NaYTiO$_4$ by the larger K and Rb ions. The $P4/nmm$ unit cell is divided into A_AO, A_RO, and TiO$_2$ layers, as illustrated in Fig. 9(a). Figure 9(b) presents the strain of the
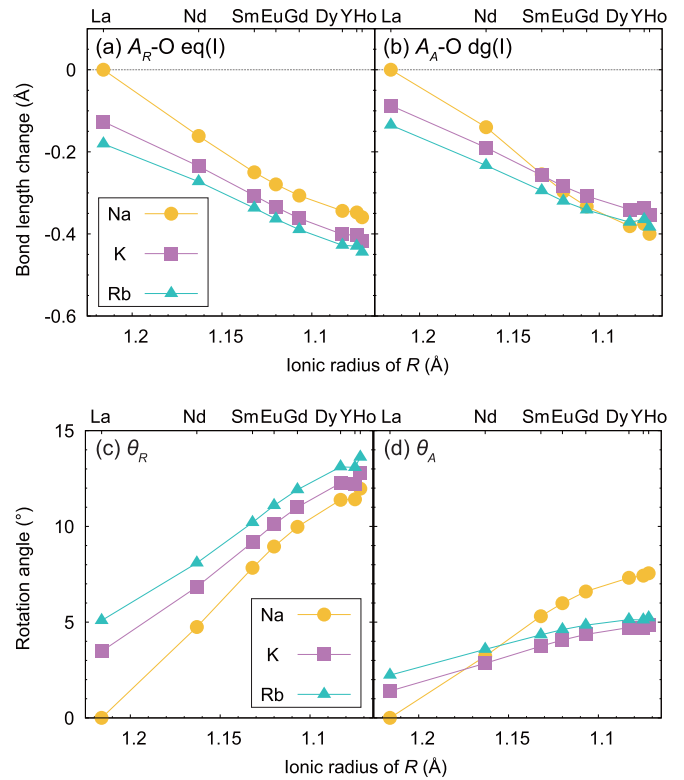
layers in KYTiO$_4$ and RbYTiO$_4$ relative to that in NaYTiO$_4$. The in-plane dimension corresponds to the in-plane lattice constants, and hence the strains are identical to each other for all the layers. These in-plane dimensions increase with increasing the radius of A_A ions because the expanded A_AO layers impose in-plane tensile strain to the A_RO and TiO$_2$ layers due to the interlayer lattice mismatch. On the other hand, the out-of-plane strains depend on the layers. With increasing A_A-ion size, the dimension of the A_AO layer simply increases, but instead the in-plane tensile strain reduces the dimension of the A_RO and TiO$_2$ layers due to Poisson effects. The out-of-plane chemical strain caused by the A_A-ion replacement can be relaxed because of the layered nature. However, the in-plane chemical strain due to the interlayer lattice mismatch cannot be fully relaxed since the layers are interfaced and clamped with each other. Here, note that the requirement to decrease the equatorial, i.e., in-plane A_R-O eq(I) bond length is responsible for the main driving force for the rotation instability as argued in the previous section (Sec. III C). The in-plane chemical tensile strain induced by incorporation of the large alkali metal ions stretches the A_R-O eq(I) bond in the $P4/nmm$ structures, and the underbonding of A_R ions increases the octahedral rotation instability leading to the $P\bar{4}2_1m$ phase.

To confirm this idea, we calculated phonon frequencies for the relevant octahedral rotation mode as a function of in-plane strain. The phonon modes become more unstable
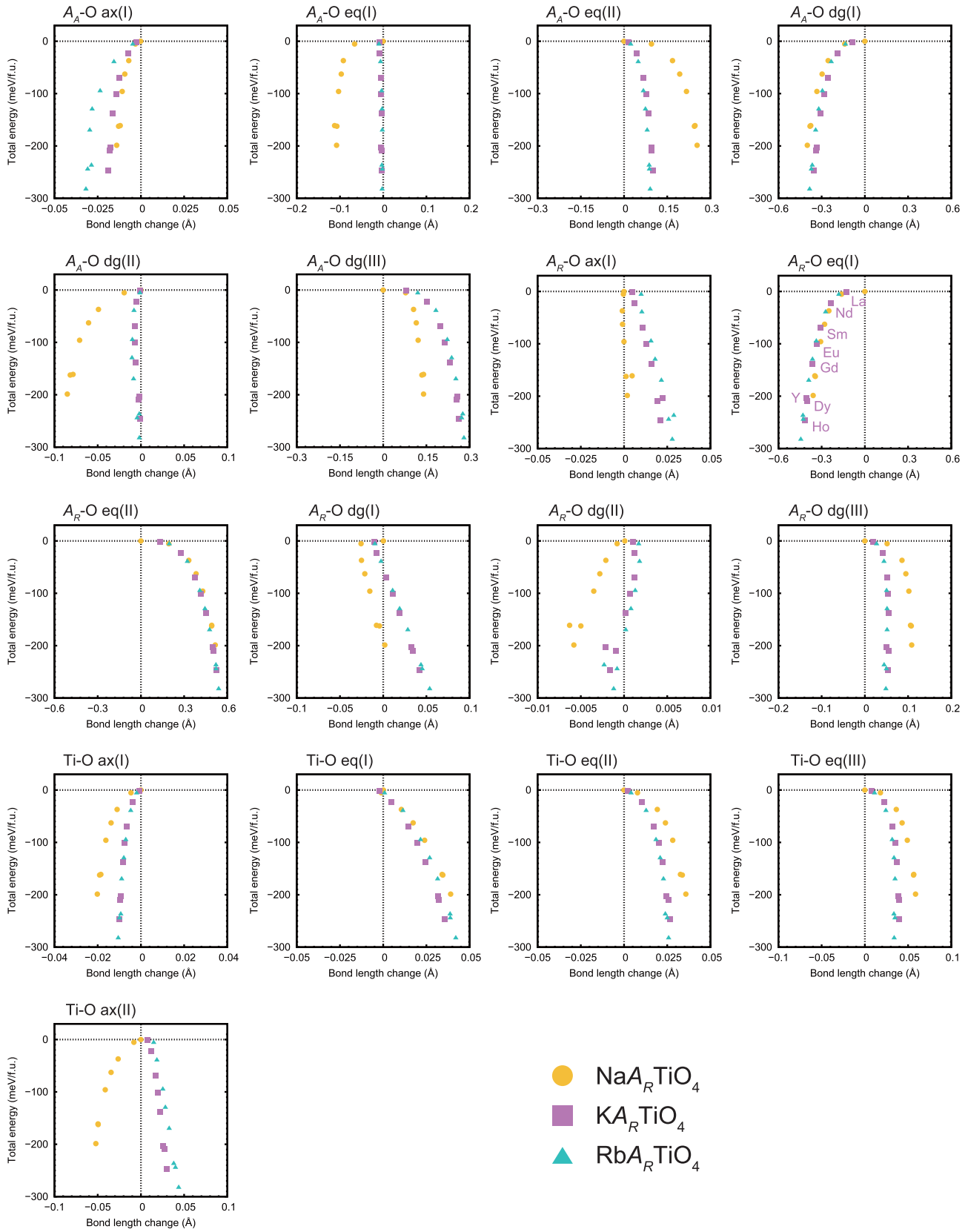
FIG. 8. Total energies of the $P\bar{4}2_1m$ structures relative to the parent $P4/nmm$ phase as a function of rotation-induced bond length change in the cation-oxygen pairs in Fig. 6(a) and for all the compositions; each panel includes the results for NaA_RTiO$_4$ (yellow circles) with A_R = La, Nd, Sm, Eu, Gd, Dy, Y, and Ho, KA_RTiO$_4$ (purple squares) with A_R = La, Nd, Sm, Eu, Gd, Dy, Y, and Ho, and RbA_RTiO$_4$ (bluish-green triangles) with A_R = La, Nd, Sm, Eu, Gd, Dy, Y, and Ho. As an example, data corresponding to each of the rare earths are labeled for the A_R-O eq(I) bonds of KA_RTiO$_4$.
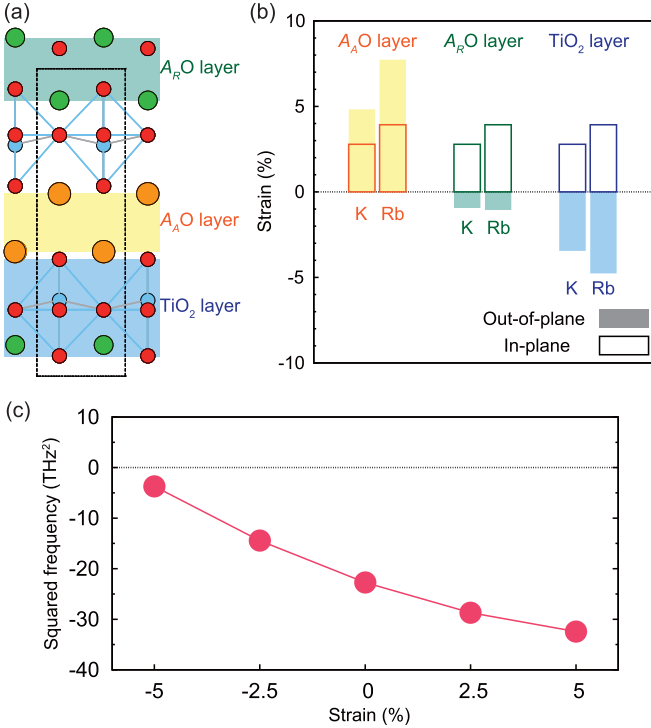
FIG. 9. (a) Schematic of the $P4/nmm$ structure, where A_AO, A_RO, and TiO$_2$ layers are highlighted. (b) Chemical strain of the layers for KYTiO$_4$ and RbYTiO$_4$ with the $P4/nmm$ structures with respect to those for NaYTiO$_4$. (c) The squared frequency of the M_1 mode for NaYTiO$_4$ with the $P4/nmm$ structure as a function of in-plane strain.

with increasing tensile strain, as shown in Fig. 9(c). Therefore, the chemical tensile strain effects due to the interlayer lattice mismatch are considered to be the origin of the effect of alkali metal size on the octahedral rotation instability.

E. Geometric descriptor

Based on our argument, the Goldschmidt tolerance factor τ cannot be treated as a descriptor for the structural instability in $A_A A_R$TiO$_4$ as it is. Mulder *et al.* reported that the energy gain obtained by the octahedral rotations in A-site ordered double perovskites $AA'B_2$O$_6$ can be described by a quadratic function of the tolerance factor [15]. For the present system, we found that the energy gain is well described by the following equation:

$$\Delta E \propto \tau_{A_A}^2 (\tau_0 - \tau_{A_R})^2, \qquad (2)$$

where τ_A is a Goldschmidt tolerance factor for a hypothetic compound ATiO$_3$, and τ_0 is a threshold value for the octahedral rotation instability. Figure 10 plots the energy gain against the right side of Eq. (2) with $\tau_0 = 0.93$. This verifies the relationship represented by Eq. (2). The threshold value less than unity is also seen in RP phases, A_3B_2O$_7$, as demonstrated by Yoshida *et al.* [30]. Note that $\tau_{A_R} \approx 0.93$ for $A_R =$ La, which is the largest rare earth, and we assume $\tau_{A_R} \geqslant 0.93$ for Eq. (2).
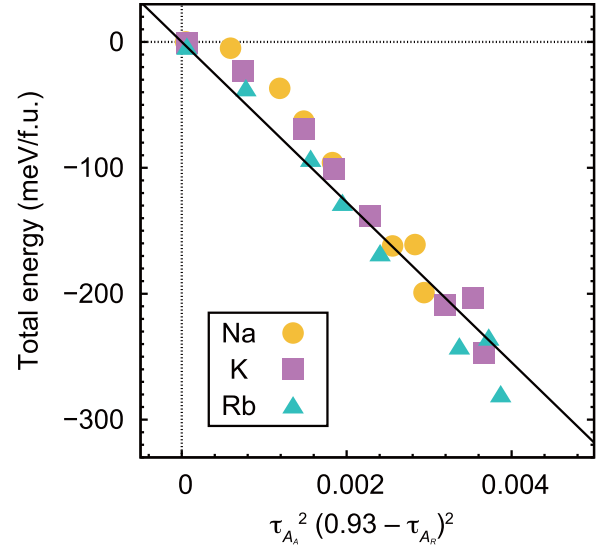

FIG. 10. Relationship between energy gain by the (Φ00)(0Φ0)-type of octahedral rotations and tolerance factors τ_A ($A = A_A$ and A_R), which is a Goldschmidt tolerance factor for a hypothetic compound ATiO$_3$.

IV. CONCLUSION

To conclude, acentricity induced by oxygen octahedral rotations represented by (Φ00)(0Φ0) is theoretically predicted through DFT calculations for A-site ordered RP alkali rare-earth titanates $A_A A_R$TiO$_4$ ($A_A =$ alkali metal, $A_R =$ rare earth), and indeed is experimentally demonstrated for KSmTiO$_4$ and KEuTiO$_4$ by means of XRD and SHG studies. The octahedral rotation instability is increased as the rare-earth ions become smaller and the alkali metal ions become *larger*. The primary driving force for the octahedral rotations is to optimize the oxygen coordination around the underbonded rare-earth ions with a high, trivalent charge. The mechanism behind the effects of alkali metal size on the rotation instability lies in tensile bond strain caused by interlayer lattice mismatch, which acts as the secondary driving force for octahedral rotations. We need to be deliberate in thinking about the octahedral rotation instability for A-site ordered layered perovskites in terms of ionic radii of A-site cations.

[1] A. M. Glazer, Acta Crystallogr., Sect. B **28**, 3384 (1972).

[2] C. J. Howard and H. T. Stokes, Acta Crystallogr., Sect. B **54**, 782 (1998).

[3] P. M. Woodward, Acta Crystallogr., Sect. B **53**, 32 (1997).

[4] N. W. Thomas, Acta Crystallogr., Sect. B **52**, 16 (1996).

[5] N. A. Benedek and C. J. Fennie, J. Phys. Chem. C **117**, 13339 (2013).

[6] P. Chen, M. N. Grisolia, H. J. Zhao, O. E. González-Vázquez, L. Bellaiche, M. Bibes, B.-G. Liu, and J. Íñiguez, Phys. Rev. B **97**, 024113 (2018).

[7] J. B. Goodenough, Rep. Prog. Phys. **67**, 1915 (2004).

[8] J. M. Rondinelli, S. J. May, and J. W. Freeland, MRS Bull. **37**, 261 (2012).

[9] A. Mercy, J. Bieder, J. Íñiguez, and P. Ghosez, Nat. Commun. **8**, 1677 (2017).

[10] V. M. Goldschmidt, Naturwissenschaften **14**, 477 (1926).

[11] E. Bousquet, M. Dawber, N. Stucki, C. Lichtensteiger, P. Hermet, S. Gariglio, J.-M. Triscone, and P. Ghosez, Nature (London) **452**, 732 (2008).

[12] N. A. Benedek and C. J. Fennie, Phys. Rev. Lett. **106**, 107204 (2011).

[13] J. M. Rondinelli and C. J. Fennie, Adv. Mater. **24**, 1961 (2012).

[14] N. A. Benedek, A. T. Mulder, and C. J. Fennie, J. Solid State Chem. **195**, 11 (2012).

[15] A. T. Mulder, N. A. Benedek, J. M. Rondinelli, and C. J. Fennie, Adv. Funct. Mater. **23**, 4810 (2013).

[16] N. A. Benedek, J. M. Rondinelli, H. Djani, P. Ghosez, and P. Lightfoot, Dalton Trans. **44**, 10543 (2015).

[17] A. Cammarata and J. M. Rondinelli, Phys. Rev. B **92**, 014102 (2015).

[18] J. Young and J. M. Rondinelli, Chem. Mater. **25**, 4545 (2013).

[19] J. Young, A. Stroppa, S. Picozzi, and J. M. Rondinelli, Dalton Trans. **44**, 10644 (2015).

[20] P. V. Balachandran, D. Puggioni, and J. M. Rondinelli, Inorg. Chem. **53**, 336 (2014).

[21] P. V. Balachandran, J. Young, T. Lookman, and J. M. Rondinelli, Nat. Commun. **8**, 14282 (2017).

[22] J. Young and J. M. Rondinelli, Phys. Rev. B **92**, 174111 (2015).

[23] M. J. Pitcher, P. Mandal, M. S. Dyer, J. Alaria, P. Borisov, H. Niu, J. B. Claridge, and M. J. Rosseinsky, Science **347**, 420 (2015).

[24] M. S. Senn, A. Bombardi, C. A. Murray, C. Vecchini, A. Scherillo, X. Luo, and S. W. Cheong, Phys. Rev. Lett. **114**, 035701 (2015).

[25] Y. S. Oh, X. Luo, F.-T. Huang, Y. Wang, and S.-W. Cheong, Nat. Mater. **14**, 407 (2015).

[26] M. E. Strayer, A. S. Gupta, H. Akamatsu, S. Lei, N. A. Benedek, V. Gopalan, and T. E. Mallouk, Adv. Funct. Mater. **26**, 1930 (2016).

[27] T. Zhu, T. Cohen, A. S. Gibbs, W. Zhang, P. S. Halasyamani, M. A. Hayward, and N. A. Benedek, Chem. Mater. **29**, 9489 (2017).

[28] T. Zhu, G. Khalsa, D. M. Havas, A. S. Gibbs, W. Zhang, P. S. Halasyamani, N. A. Benedek, and M. A. Hayward, Chem. Mater. **30**, 8915 (2018).

[29] S. Yoshida, K. Fujita, H. Akamatsu, O. Hernandez, A. Sen Gupta, F. G. Brown, H. Padmanabhan, A. S. Gibbs, T. Kuge, R. Tsuji *et al.*, Adv. Funct. Mater. **28**, 1801856 (2018).

[30] S. Yoshida, H. Akamatsu, R. Tsuji, O. Hernandez, H. Padmanabhan, A. Sen Gupta, A. S. Gibbs, K. Mibu, S. Murai, J. M. Rondinelli *et al.*, J. Am. Chem. Soc. **140**, 15690 (2018).

[31] H. Akamatsu, K. Fujita, T. Kuge, A. Sen Gupta, A. Togo, S. Lei, F. Xue, G. Stone, J. M. Rondinelli, L.-Q. Chen *et al.*, Phys. Rev. Lett. **112**, 187602 (2014).

[32] A. S. Gupta, H. Akamatsu, M. E. Strayer, S. Lei, T. Kuge, K. Fujita, C. dela Cruz, A. Togo, I. Tanaka, K. Tanaka *et al.*, Adv. Electron. Mater. **2**, 1500196 (2016).

[33] A. Sen Gupta, H. Akamatsu, F. G. Brown, M. A. T. Nguyen, M. E. Strayer, S. Lapidus, S. Yoshida, K. Fujita, K. Tanaka, I. Tanaka *et al.*, Chem. Mater. **29**, 656 (2017).

[34] S. K. Aleksandrov, Crystallogr. Rep. **40**, 251 (1995).

[35] M. C. Knapp, Ph.D. thesis, The Ohio State University, 2006.

[36] R. E. Schaak and T. E. Mallouk, J. Solid State Chem. **161**, 225 (2001).

[37] B.-C. Zhu and K.-B. Tang, Acta Crystallogr., Sect. E **67**, i26 (2011).

[38] N. Zhang, C. Guo, J. Zheng, X. Su, and J. Zhao, J. Mater. Chem. C **2**, 3988 (2014).

[39] P. E. Blöchl, Phys. Rev. B **50**, 17953 (1994).

[40] G. Kresse and D. Joubert, Phys. Rev. B **59**, 1758 (1999).

[41] J. P. Perdew, A. Ruzsinszky, G. I. Csonka, O. A. Vydrov, G. E. Scuseria, L. A. Constantin, X. Zhou, and K. Burke, Phys. Rev. Lett. **100**, 136406 (2008).

[42] J. P. Perdew, K. Burke, and M. Ernzerhof, Phys. Rev. Lett. **77**, 3865 (1996).

[43] J. P. Perdew, K. Burke, and M. Ernzerhof, Phys. Rev. Lett. **78**, 1396 (1997).

[44] G. Kresse and J. Hafner, Phys. Rev. B **48**, 13115 (1993).

[45] G. Kresse and J. Hafner, Phys. Rev. B **47**, 558 (1993).

[46] G. Kresse and J. Furthmüller, Comput. Mater. Sci. **6**, 15 (1996).

[47] G. Kresse and J. Furthmüller, Phys. Rev. B **54**, 11169 (1996).

[48] A. Togo and I. Tanaka, Scr. Mater. **108**, 1 (2015).

[49] A. Togo and I. Tanaka, Phys. Rev. B **87**, 184104 (2013).

[50] F. Izumi and K. Momma, Solid State Phenom. **130**, 15 (2007).

[51] See Supplemental Material at http://link.aps.org/supplemental/10.1103/PhysRevMaterials.3.065001 for treelike diagrams summarizing the stable structure exploration for $KYTiO_4$ and $RbYTiO_4$.

[52] R. D. Shannon, Acta Crystallogr., Sect. A **32**, 751 (1976).

[53] P. V. Balachandran, A. Cammarata, B. B. Nelson-Cheeseman, A. Bhattacharya, and J. M. Rondinelli, APL Mater. **2**, 076110 (2014).

[54] B. B. Nelson-Cheeseman, H. Zhou, P. V. Balachandran, G. Fabbris, J. Hoffman, D. Haskel, J. M. Rondinelli, and A. Bhattacharya, Adv. Funct. Mater. **24**, 6884 (2014).